Impact of Zn addition on structural, morphological, and magnetic properties of thermally annealed Li–Zn nanoferrite

S N Kane, R. Verma, C. Parmar, S S Modak, J P Araujo, Frédéric Mazaleyrat, Tetiana Tatarchuk

Impact of Zn addition on structural, morphological, and magnetic properties of thermally annealed Li–Zn nanoferrite

S. N. Kane[a], R. Verma[a], C. Parmar[a], S. S. Modak[a], J. P. Araujo[b], F. Mazaleyrat[c], Tetiana Tatarchuk[d,e]*

[a]*Magnetic Materials Laboratory, School of Physics, D. A. University, Khandwa Road Campus, Indore-452001, India*

[b]*IFIMUP, Departmento de Fisica, Universidade de Porto, 4169-007 Porto, Portugal*

[c]*SATIE, ENS Paris-Saclay, Gif-sur-Yvette, France*

[d]*Faculty of Chemistry, Jagiellonian University, 30-387 Kraków, Poland*

[e]*Educational and Scientific Center of Materials Science and Nanotechnology, Vasyl Stefanyk Precarpathian National University, 76018 Ivano-Frankivsk, Ukraine*

CONTACT S. N. Kane, kane_sn@yahoo.com, Magnetic Materials Laboratory, School of Physics, D. A. University, Khandwa Road Campus, Indore-452001, India

Tetiana Tatarchuk, tatarchuk.tetyana@gmail.com, Faculty of Chemistry, Gronostajova str., 2, Jagiellonian University, 30-387 Kraków, Poland; Educational and Scientific Center of Materials Science and Nanotechnology, Vasyl Stefanyk Precarpathian National University, Shevchenko str., 52, 76018 Ivano-Frankivsk, Ukraine

Impact of Zn addition on structural, morphological, and magnetic properties of thermally annealed Li–Zn nanoferrite

The effect of Zn addition on cationic distribution, structural properties, magnetic properties, and antistructural modeling of nanocrystalline Li-Zn ferrites are reported. X-ray diffraction (XRD) confirms the formation of single-phase cubic spinel nanoferrites with an average grain diameter of 34–82 nm. The addition of Zn ions results in a linear increase of lattice parameter a_{exp} and X-ray density ρ_{XRD} related to substitution by an ion with a higher ionic radius ($r(Zn^{2+}) > r(Li^{+})$). Magnetism in the studied samples is governed by the Yafet-Kittel (Y−K) three-sub-lattice model, shown by a non-zero canting angle, ranging between 7.02 – 39.21 degrees. Agglomerated non-uniform particle distribution is observed in scanning electron microscope images. The observed variation in magnetic properties is correlated with the calculated cationic distribution. A new antistructural modeling for describing active surface centers is discussed. The antistructural modeling explains the changes in the concentration of donor and acceptor surface active centers.

Keywords: lithium-zinc ferrite; auto-combustion; XRD; cation distribution; antistructural modeling.

1. Introduction

Magnetic materials such as spinel ferrites are widely used in many electronic devices and, therefore, attract a lot of attention from researchers due to their interesting physical properties. AB_2O_4 is the general molecular formula of ferromagnetic spinel ferrites, exhibiting a face-centered cubic structure with two inter-penetrating sub-lattices tetrahedral A (occupied by a divalent metal ion Mg^{2+}, Zn^{2+}, Fe^{2+}, Co^{2+}, etc.), and octahedral B (occupied by trivalent metal ion Al^{3+}, Fe^{3+}, Cr^{3+}, etc.) [1]. It is well known that the magnetic properties of ferrites strongly depend on the chemical composition, and method of their preparation. At the same time, producing ferrites at the nanoscale is also important. Therefore, synthesis technique, ferrite composition, post-preparation thermal treatment, grain diameter, cationic distribution, etc. can be effectively used for tuning

their magnetic properties [2–10], thus making them valuable for various applications including those in − high density recording, targeted drug delivery applications, in high frequency applications, gas sensing, magnetic resonance imaging MRI.

Different spinel ferrites have been widely investigated during the last years, and the influence of various transition and rare earth metal ions doping on the properties of ferrites has been described. A small amount of substituted ions in ferrites can dramatically change their properties. Among spinel ferrites the lithium and cation-substituted lithium ferrites are promising materials as microwave absorbers due to their good chemical and thermal stability, high magnetization, high electrical resistivity, superparamagnetism, and low cost [11-16]. The lithium ferrite $Li_{0.5}Fe_{2.5}O_4$ has an inverse spinel structure, while $ZnFe_2O_4$ has a normal spinel structure, so Li-Zn ferrite would display a mixed spinel structure. Therefore, a controlled Zn-addition in Li-ferrite will lead to a systematic modification of the distribution of cations on the A, and B sites, and there would be a transformation from an inverse spinel to a mixed spinel, which in turn will have a visible effect on magnetic properties. Use of X-ray diffraction 'XRD', combined with magnetic measurements respectively would be of help in understanding the modification of cationic distribution, its effect on magnetic properties, and the correlation between them.

It is worth noting that, the magnetic properties of nanoferrites differ from their bulk counterparts due to size dependence e. g. [17], and in nanoparticles, the large surface-to-volume ratio leads to dissimilar distribution of cations on A, B site as compared to their bulk counterparts. Magnetic and electric properties of lithium-substituted ferrites can be improved by the substitution of octahedral Fe^{3+} ions by rare earth ions such as Gd [18, 19], Dy [20-22], Pr [23], La [24, 25], Tb [26], Ho [27], Nd [28], Gd / Er [29]. It was shown that introducing rare earth ions into the spinel lattice leads to a change in both the electrical, and magnetic behavior of ferrites.

In the case of lithium ferrite, one can observe the substitution $Me^{2+} = 0.5Li^{+} + 0.5Fe^{3+}$. Therefore, the physical and chemical properties of ferrites depend upon their chemical composition and cation distribution in tetrahedral (A) and octahedral (B) sites. Lithium ferrites have become attractive these days due to their technological applicability. In addition, the Curie temperature of Li ferrite is highest in spinels reaching a value of 958 K [30]. Many researchers have investigated the impact of the synthesis conditions on the particle size, morphology, electric, magnetic, dielectric, and microwave properties of the spinel ferrites. Numerous methods can be used for obtaining spinel ferrites, such as the conventional ceramic method [31], mechanical milling [32], hydrothermal method [33], chemical co-precipitation method [34], sol-gel auto combustion synthesis [35-39], microwave-solvothermal method [40], green synthesis [41]. Compared to other methods, the sol-gel auto combustion method has many advantages for the lithium ferrites as they can be obtained in a shorter time, at lower temperatures and these prevent loss of lithium during the synthesis process [42, 43].

Aravind *et al.* [44] prepared nanocrystalline lithium-cobalt ferrites $[Li_{0.5}Fe_{0.5}]_{1-x}Co_xFe_2O_4$ (where x = 0.0, 0.2, 0.4, 0.6, 0.8, and 1.0) with the crystallite sizes ranging from 37 to 43 nm, which were synthesized at lower processing temperature (180 ^{o}C) by non-conventional citrate gel auto-combustion method using citric acid as a fuel. The thermoelectric power studies demonstrated that with Co-substitution at low temperatures, ferrites demonstrate the p-type semiconducting behavior, and at higher temperatures, they act like n-type semiconductors. The magnesium ions were incorporated into lithium-zinc ferrite $Li_{0.1}Zn_{0.8}Fe_{2.1}O_4$ by Sun *et al.* [45] and the samples were annealed at 750, 900, 1050, and 1200 ^{o}C for 6 h. The crystallite sizes were in the range of 50 – 90 nm. Borhan *et al.* [46] reported nanocrystalline Li–Zn ferrites $Li_{0.5}Zn_xFe_{2.5-x}O_4$ (where x = 0, 0.1, 0.2, 0.3, 0.4, 0.5) with the particle size of 20 – 40 nm, which were synthesized by the

microwave glycine–nitrate process. It was investigated that maximum saturation magnetization and magnetic permeability were obtained for the sample with x = 0.2. Nanocrystalline lithium-zinc ferrites substituted with cobalt $Li_{0.4-0.5x}Zn_{0.2}Co_xFe_{2.4-0.5x}O_4$ (where $0.0 \leq x \leq 0.1$) were synthesized by the citrate precursor method by Soibam *et al.* [47]. The maximal saturation magnetization was observed for x = 0.02 and the cobalt has shown anomalous behavior when substituted in lithium ferrites in the presence of Zn. Ruiz *et al.* [48] presented the effect of Al substitution on the magnetic and electrical properties of $Li_{0.2}Zn_{0.6}Fe_{2.2-x}Al_xO_4$ ferrites ($0.0 \leq x \leq 0.5$) prepared by the standard ceramic technique. The application range of the substituted samples increases from 1 MHz (x=0.0) to 50 MHz (x=0.5) although the magnetic permeability values decrease with the substitution of aluminum. It was shown that attenuation has a maximum intensity (86 dB) near 90 MHz for x=0.4. The effect of Si addition on the structure and electrical properties of lithium ferrite was also explored [49]. Polycrystalline Li-Si ferrites with the general chemical formula $Li_{0.5+0.5x}Si_xFe_{2.5-1.5x}O_4$ (where x = 0.0, 0.1, 0.2, 0.3, 0.4, 0.5 and 0.6) were prepared by high energy ball milling (HEBM) technique. The possible mechanism for the influence of silicon substitution on the electrical properties of lithium ferrites was discussed based on the hopping and small polaron models. However, Li-Zn ferrites have a problem in the sintering process, as at high temperatures lithium volatilization from the sample and further deterioration of the electromagnetic properties take place [50]. Hence, the temperature of the synthesis process for lithium-zinc ferrites must be decreased without deteriorating magnetic properties. Thus, for synthesizing Li-based ferrites, sol-gel auto-combustion method is better suited, which utilizes relatively lower-temperature ~110 ^oC during synthesis process.

It is of value to note that literature [3] reports Zn-content dependence of structural, magnetic properties of Li-Zn based ferrite in dry gel form dry gel *i.e.* without any post-

preparation thermal treatment, whereas this work reports matching composition as that of [3], nevertheless the present work certainly contains following newer information: i) prepared dry gel samples are thermally-treated to study the thermal-treatment-induced modification of cationic distribution, grain diameter, which will have effect on A-O-B, B-O-B, A-O-A super-exchange interaction, thus affecting magnetic properties; ii) deeper analysis of the structural, magnetic data, and correlation between them; iii) scanning electron microscopy (SEM) images, particle size distribution, and its interpretation; iv) Antistructure modelling was also done to get information about the nature of the surface active centers [31,34]. This approach provides valuable information about the physical and chemical properties of crystalline materials, helping to identify the nature and concentration of point defects, which are crucial in determining various material properties such as electrical, magnetic, or catalytic activity. Additionally, the antistructure model enables the prediction of technology for materials with specific defect concentrations.

Thus, the objective of the present work is to report our work on sol-gel auto-combustion synthesis of Zn-added lithium ferrites: $Li_{0.5-x/2}Zn_xFe_{2.5-x/2}O_4$ ($0.0 \leq x \leq 1.0$), using citrate-nitrate-acetate precursors. XRD, magnetic measurements were used to study structural, and magnetic properties, and the correlation between them. SEM images provide information about particle size; particle-size distribution, and morphology. Antistructure modelling was also done to get information about the nature of the surface active centers of the obtained samples were investigated.

2. Experimental

2.1. Samples synthesis

Zinc-added lithium ferrites of nominal composition $Li_{0.5-x/2}Zn_xFe_{2.5-x/2}O_4$ ($0.0 \leq x \leq 1.0$)

in powder form were prepared by the sol-gel auto combustion method. Following citrate-nitrate/acetate precursors were used in the synthesis: zinc nitrate $Zn(NO_3)_2 \cdot 6H_2O$, ferric nitrate $Fe(NO_3)_3 \cdot 9H_2O$, lithium acetate $Li(CH_3COO) \cdot 2H_2O$ and citric acid $C_6H_8O_7$. The precursors were mixed in stoichiometric ratio. Citric acid was used as 'fuel' and the metal salts to fuel ratio is taken as 1:1. In the beginning, citric acid acts as a chelating agent for metal ions, which helps in preventing their selective precipitation to maintain compositional homogeneity among the constituents. Afterward, it also serves as a fuel in the combustion reaction. To start the synthesis process, all the precursor materials were dissolved in de-ionized water in a beaker under constant stirring to get a homogeneous solution. The pH was maintained at 7 by adding an ammonia solution. Then the solution was heated at ~ 110 ^{o}C in the air till fluffy power was formed called 'dry gel' or as-burnt powder, which was then annealed at 450 °C for 3 h, and used for XRD, magnetic measurements, and SEM measurements. The chemical reactions involved in the period of the synthesis process can be expressed as follows:

$$(2\text{-}2x)Li(CH_3COO)_{(aq)} + 4xZn(NO_3)_{2(aq)} + (10\text{-}2x)Fe(NO_3)_{3(aq)} + 12C_6H_8O_{7(aq)} + (62.5\text{-}6.5x)O_2 \rightarrow$$

$$\xrightarrow{+NH_4OH\ (pH=7)} 4Li_{0.5-x/2}Zn_xFe_{2.5-x/2}O_{4(s)} + (76\text{-}4x)CO_{2(g)} + (15+x)N_{2(g)} + (51\text{-}3x)H_2O_{(g)}$$

2.2. Samples characterization

XRD measurements were done at room temperature by using Bruker D8 advance diffractometer with CuK_α radiation ($\lambda = 0.15418$ nm). The X-ray diffraction patterns were recorded in the angular range $20° \leq 2\theta \leq 70°$ with a step size of 0.02°. Hysteresis measurements were done using a Lakeshore Model 7410 Vibration Sample Magnetometer (VSM) by applying maximum field $H_{max} \approx \pm 1.8$ Tesla**.** The surface

morphology of the studied samples was done by a field emission scanning electron microscope (FE-SEM) (FEI Quanta 400FEG).

2.3. Analysis of the data

XRD patterns were analyzed to compute structural parameters: experimental lattice parameter '$a_{exp.}$' (*making use of (311) reflection*), x-ray density (ρ_{xrd}) as described in [5]. By incorporating both instrumental broadening (*obtained by taking XRD data of standard LaB_6 sample*), and strain broadening, grain diameter ($D_{W\text{-}H}$), and strain (ε) were obtained by using Williamson Hall (W-H) method [5]. Dislocation density (ρ_D), and specific surface area (S) were calculated by using the value of grain diameter ($D_{W\text{-}H}$) as described in [5, 8]. Cationic distribution was computed by the Bertaut method [51]. It provides cationic distribution on A, and B sites by comparing experimental, evaluated intensity ratios for (200), (400), and (422) planes, as given in [52]. The intensity ratio: $I_{(220)}/I_{(440)}$, $I_{(400)}/I_{(422)}$, $I_{(220)}/I_{(400)}$ differs for different cation distributions on A, and B sites. Optimal distribution of cations on the A and B-site for which theoretical, experimental ratios (I_{hkl}^{Calc} and I_{hkl}^{Obs}) of the calculated, observed intensities agree noticeably, is taken. Bond angles ($\theta_1, \theta_2, \theta_3, \theta_4, \theta_5$), Oxygen position parameter (u), and inversion parameter (δ) i. e Fe^{3+} ions on A-site, were also computed from cationic distribution, as detailed in [53]. Obtained cationic distribution was used to compute Néel magnetic moment '$\mathbf{n_N}$', theoretical magnetization at 0 K: $M_{s(th)}$. Saturation magnetization M_s, Remanence M_r, Coercivity H_c reduced remanence M_r/M_s were obtained from hysteresis measurements. Hysteresis loops were also used to compute the magnetization derivatives dM/dH. ImageJ software [54] was used to analyze SEM images to get particle size distribution. Various expressions used for calculating XRD, magnetic parameters are given in supplementary materials.

3. Results and Discussion

3.1 Structural properties

Fig. 1 shows the XRD patterns of the studied samples, confirms the formation of nanocrystalline spinel phase with grain diameter ranging between 34 nm to 82 nm, and shows the presence of characteristic spinel ferrite peaks diffraction peaks corresponding to (220), (311), (222), (400), (422),(511), (440) planes (JCPDS card number: 73-2410). The left inset of Fig. 1 shows the expanded view of (311) peak, which shifts to higher two theta values, revealing that with increasing Zn-content lattice parameter $a_{exp.}$ increases (see right inset of Fig. 1), indicates the expansion of the unit cell, described by experimental relation: $a_{exp.}$ = 0.005[Zn-content] + 0.836. The increase of $a_{exp.}$ is attributable to the fractional replacement of Li ion with an ionic radius of 0.068 nm by Zn ion whose ionic radius is 0.074 nm. Modification of X-ray density (ρ_{XRD}) is also observed, and it varies between 4763.7 to 5336.1 kg/m^3 and is consistent with the change in $a_{exp.}$ A perusal of Fig. 1 also reveals that except for sample with x = 0.9, 1.0, where ~ 3% Fe_2O_3 phase (JCPDS Card number: 39-1346) was also observed is ascribable to rather low thermal annealing temperature ~450^{o}C [55-56] was observed via XRD data, while rest is spinel ferrite phase, for all the other samples. It is worth noting that, the antiferromagnetic nature of Fe_2O_3 is expected to influence the saturation magnetization $M_{s(exp.)}$ or M_s of the samples with x = 0.9; 1.0.

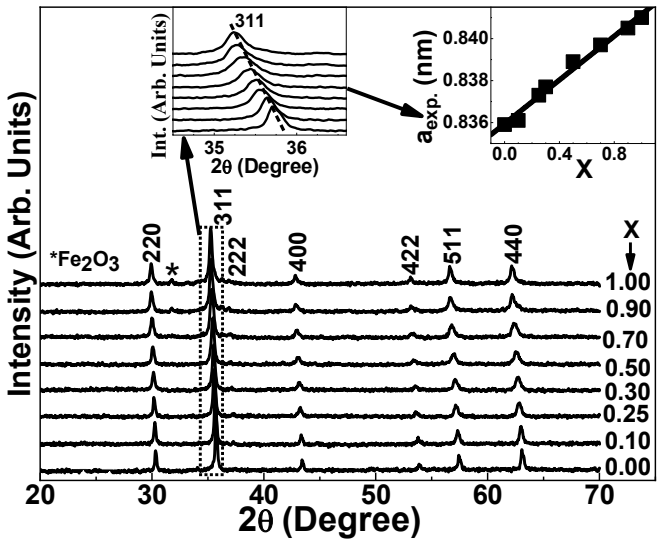

Figure 1. XRD patterns of the studied samples (Left inset: expanded view of 311 peak, Right inset: $a_{exp.}$ dependence, for the studied samples).

Table 1. Cationic distribution (for *A* and *B-site*), and calculated, observed value of intensity ratios I_{220}/I_{440}, I_{400}/I_{422}, I_{220}/I_{440}.

x	Cation Distribution	I_{220}/I_{440}		I_{400}/I_{422}		I_{220}/I_{440}	
		Calc.	Obs.	Calc.	Obs.	Calc.	Obs.
0.0	$(Zn_{0.00}^{2+}Li_{0.07}^{1+}Fe_{0.93}^{3+})^{A}[Zn_{0.00}^{2+}Li_{0.43}^{1+}Fe_{1.57}^{3+}]^{B}$	0.9705	1.1214	1.8070	1.8661	1.9611	2.0578
0.1	$(Zn_{0.00}^{2+}Li_{0.00}^{1+}Fe_{1.00}^{3+})^{A}[Zn_{0.10}^{2+}Li_{0.45}^{1+}Fe_{1.45}^{3+}]^{B}$	0.9476	1.0244	1.7481	1.6175	1.9851	2.0576
0.25	$(Zn_{0.10}^{2+}Li_{0.05}^{1+}Fe_{0.85}^{3+})^{A}[Zn_{0.15}^{2+}Li_{0.325}^{1+}Fe_{1.525}^{3+}]^{B}$	0.8928	1.0028	1.8292	1.8315	1.9882	2.0626
0.3	$(Zn_{0.13}^{2+}Li_{0.05}^{1+}Fe_{0.82}^{3+})^{A}[Zn_{0.17}^{2+}Li_{0.30}^{1+}Fe_{1.53}^{3+}]^{B}$	0.9689	1.0601	1.8583	1.8736	1.9655	2.0291
0.5	$(Zn_{0.20}^{2+}Li_{0.00}^{1+}Fe_{0.80}^{3+})^{A}[Zn_{0.30}^{2+}Li_{0.25}^{1+}Fe_{1.45}^{3+}]^{B}$	0.9618	1.1195	1.6748	1.7025	1.9729	2.0412
0.7	$(Zn_{0.15}^{2+}Li_{0.05}^{1+}Fe_{0.80}^{3+})^{A}[Zn_{0.55}^{2+}Li_{0.10}^{1+}Fe_{1.35}^{3+}]^{B}$	0.9619	1.0723	2.1773	1.9810	1.9692	2.1033
0.9	$(Zn_{0.10}^{2+}Li_{0.00}^{1+}Fe_{0.90}^{3+})^{A}[Zn_{0.80}^{2+}Li_{0.05}^{1+}Fe_{1.15}^{3+}]^{B}$	0.9.09	1.0254	2.1793	1.9624	1.9849	2.1545
1.0	$(Zn_{0.09}^{2+}Li_{0.00}^{1+}Fe_{0.91}^{3+})^{A}[Zn_{0.91}^{2+}Li_{0.00}^{1+}Fe_{1.09}^{3+}]^{B}$	0.9838	1.1202	2.0712	1.9808	1.9680	2.1048

Table 1 gives cationic distribution on ***A***, ***B-site***, and calculated, observed value of intensity ratios I_{220}/I_{440}, I_{400}/I_{422}, I_{220}/I_{440}. Perusal of Table 1 shows that as we increase Zn-content, on B-site: there is reduction of the population of Fe^{3+} ions, Li^{1+} ions with a

simultaneous increase of Zn^{2+} ions. Table 1 also suggests that Li^{1+}, Zn^{2+}, Fe^{3+}, ions reside on both A, and B sites, but Li^{+}, Zn^{2+} ions are more populated on B-site than A-site. Observed modification of cationic distribution is ascribable to thermal-annealing assisted movement of, Li^{1+}, Zn^{2+}, and Fe^{3+}, cations on A, and B sites [56-57], and would affect magnetic properties, and is explained later. Close agreement of: i) Calc., Obs. intensity ratios - I_{220}/I_{440}, I_{400}/I_{422}, I_{220}/I_{440}, shown in Table 1, and ii) $a_{th.}$ (*range between 0.8359 nm–0.8410 nm*), $a_{exp.}$ (*range between 0.8327 – 0.8435 nm*) corroborate the reliability of the computed cation distribution.

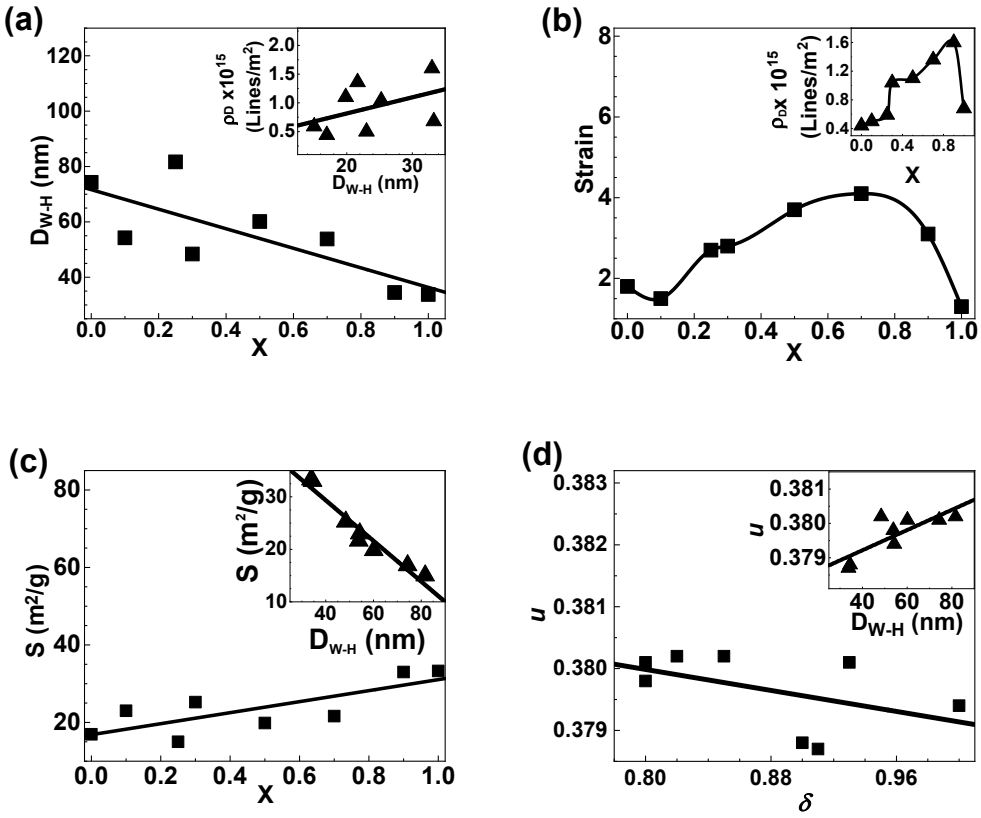

Figure 2. Zn-content dependence of: (**a**) grain diameter (Inset: variation of dislocation density with grain diameter), (**b**) strain (Inset: variation of dislocation density with Zn-content), (**c**) Specific surface area (Inset: variation of specific surface area with grain diameter), (**d**) Variation of oxygen parameter with degree of inversion (Inset: variation of Oxygen parameter with grain diameter).

Fig. 2a depicts the Zn-content dependence of $D_{W\text{-}H}$, described by the following experimental relation: $D_{W\text{-}H}$ = 71.648 – 35.308 (Zn-content). Fig. 2a (inset) shows an increase in dislocation density (ρ_D). The decrease of $D_{W\text{-}H}$ with Zn-content is attributable to: i) fractional replacement of Li^+ ion with lower ionic radius by Zn^{2+} ion with higher ionic radius; ii) increase of grain boundary curvature [58], associated with changes in lattice parameter. Fig. 2b depicts the variation of strain with Zn-content, which is ascribable to composition-dependent variation of the cationic distribution shown in Table 1, where modification of population of Li^+, Zn^{2+}, Fe^{3+}, cations on A, B site is observed. Inset (Fig. 2b) shows the variation of dislocation density (ρ_D) with Zn-content and is congruent with the obtained strain, $a_{exp,}$ and $D_{W\text{-}H}$ data. Fig. 2c shows a linear increase of compositional-dependent specific surface area (S) described by experimental relation: S = 14.207 [Zn-content] + 16.841, attributed to corresponding changes in ρ_{XRD}, $D_{W\text{-}H}$. Fig. 2b(inset) describes the variation of S with $D_{W\text{-}H}$, attributed to the well-known inverse relationship between S and $D_{W\text{-}H}$ [8], described by experimental relation: S = 44.786 − 0.7386 [$D_{W\text{-}H}$]. A perusal of Fig. 2d displays a decrease of u with δ, ascribable to the variation of disorder via modification of cationic distribution (see Table 1), as was also reported in [7, 8]. In the studied samples, u varies between 0.3787 − 0.3802, which is higher than its ideal value of 0.375 [53], revealing enhanced disorder as compared to perfect spinel structure, and hence should be reflected in magnetic properties [53]. As is known that Li-ferrite shows inverse spinel structure, and Zn-ferrite has normal spinel structure, so Zn-addition in Li-ferrite would lead to changes in the inversion degree δ. In the studied samples, with Zn-addition the δ varies between 0.8 − 1.0, shows that the spinel structure transforms from inverse-spinel to mixed-spinel. Inset of Fig. 2d shows linear increase of oxygen parameter with grain diameter is attributable to compositional

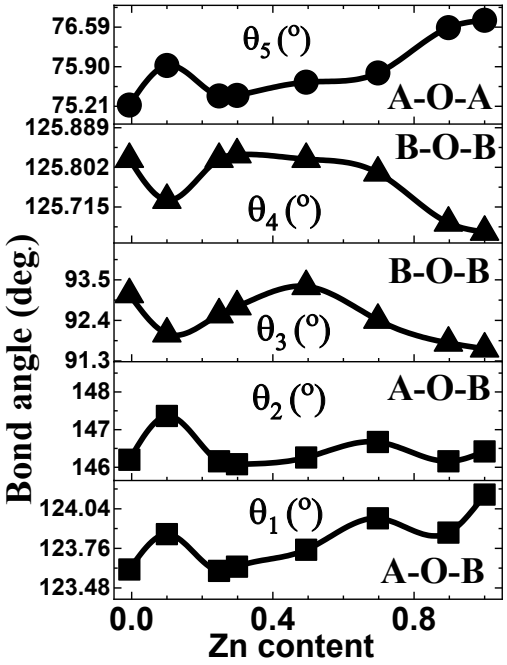

Figure 3. Bond angle variation for the studied samples. Line connecting points are a guide to the eye.

dependence of cationic distribution shown in Table 1 [8], and described by the following experimental relation: u = 2.9177e-5(D_{W-H}) + 0.378.

Figure 3 depicts the variation of bond angles with increasing Zn-content. It is worth noting that, bond angles are closely related to the strength of A-O-B, B-O-B and, A-O-A super-exchange interaction [59], and bond angles θ_1, θ_2 reveal information on A-O-B, θ_3, θ_4 provide information on B-O-B and, θ_5 gives information on A-O-A super-exchange interaction [2, 5, 8-9, 59]. Perusal of Fig. 3 shows that with increasing Zn-content, increase of θ_1, θ_2, θ_5 suggests strengthening of A-O-B, A-O-A interaction through concurrent decrease of θ_3, θ_4 suggests weakening of B−O−B interaction, and would reveal changes in magnetic properties is consistent with earlier studies e. g. in − [5, 9].

3.2 Antistructural Modeling

Many of the important properties of ionic crystals are influenced and often determined by the defect structure and particularly by the properties of the surface of solids. Antistructural modeling is a very promising approach in solid-state chemistry since it gives fundamentally vital new information about the physical and chemical properties of crystalline materials [60]. It helps to define the nature and concentration of point defects, which often determine the properties (electrical, magnetic, optical, reactivity, catalytic activity, etc.). The antistructure model makes it possible to establish the nature of the active centers of adsorption and predict the technology of materials with a given concentration of defects [60-61].

In this work, a defect modeling for the Li-Zn ferrite systems and the surface active centers are described. The presented results offer interesting insights into the solid-state chemistry of the Li-Zn ferrites. The antistructural model for the Li-Zn ferrite systems is constructed upon crystal-chemical composition and spinel antistructure (which can be given from perfect spinel structure $MgAl_2O_4$ [62]). In this perfect spinel, Mg^{2+} ions occupy perfect tetrahedral (A) positions and Al^{3+} ions occupy perfect octahedral (B) sites. In Kroëger–Vink notation, the quasichemical reaction for perfect spinel can be represented as:

$$\mathrm{Mg_A^{\times}}\left[\mathrm{Al_2^{\times}}\right]_{\mathrm{B}}\left(\mathrm{O_4^{\times}}\right)_{\mathrm{O}} \rightarrow \mathrm{Mg^{2+}} + 2\mathrm{Al^{3+}} + 4\mathrm{O^{2-}} + \underbrace{\mathrm{V_A''}\left[\mathrm{V_2'''}\right]_{\mathrm{B}}\left(\mathrm{V_4^{\bullet\bullet}}\right)_{\mathrm{O}}}_{\text{spinel antistructure}}$$

where ● is an excess positive charge, '' is a double excess negative charge, $^{\times}$ is an effective zero charge, V is the vacancy, A is a tetrahedral site, B is an octahedral site, and O is the anion site. With the Kröger-Vink notation, in the spinel antistructure negatively charged cation vacancies V_A'' and V_B''' are treated as charge balancing vacancies to the positively charged anion (oxygen) vacancies.

The chemical composition of the Li-Zn ferrite system (Table 2) does not give any information about the active centers on the surface of spinel ferrites, but an antistructural model takes into account the presence of donor and acceptor active centers on the surface of solids. The antistructural model gives a better understanding of the formation, nature, and role of lattice defects in the different processes [60]. The antistructural mechanism provides a superposition of crystal structure with spinel antistructure $V_A''[V_2''']_B(V_4^{\bullet\bullet})_O$. Detailed explanations of the interaction between cations and vacancies are next:

for A-site:

$$Li_A^+ + V_A'' \rightarrow Li_A'$$

$$Zn_A^{2+} + V_A'' \rightarrow Zn_A^{\times}$$

$$Fe_A^{3+} + V_A'' \rightarrow Fe_A^{\bullet}$$

for B-site:

$$Li_B^+ + V_B''' \rightarrow Li_B''$$

$$Zn_B^{2+} + V_B''' \rightarrow Zn_B'$$

$$Fe_B^{3+} + V_B''' \rightarrow Fe_A^{\times}$$

Antistructural modeling for some of the Li-Zn ferrites can be written as follows:

for x=0.00:

$$\left(Li_{0.07}^{+}Fe_{0.93}^{3+}\right)_A\left[Li_{0.43}^{+}Fe_{1.57}^{3+}\right]_B\left(O_4^{2-}\right)_O + \underbrace{V_A''[V_2''']_B\left(V_4^{\bullet\bullet}\right)_O}_{\text{spinel antistruct ure}} \rightarrow$$

$$\rightarrow \underbrace{\left(Li_{0.07}'Fe_{0.93}^{\bullet}\right)_A\left[Li_{0.43}''Fe_{1.57}^{\times}\right]_B\left(O_4^{\times}\right)_O}_{\text{lithium ferrite}}$$

for x=0.50:

$$\left(Zn_{0.20}^{2+}Fe_{0.80}^{3+}\right)_A\left[Li_{0.25}^{+}Zn_{0.30}^{2+}Fe_{1.45}^{3+}\right]_B\left(O_4^{2-}\right)_O + \underbrace{V_A''[V_2''']_B\left(V_4^{\bullet\bullet}\right)_O}_{\text{spinel antistruct ure}} \rightarrow$$

$$\underbrace{\left(Zn_{0.20}^{\times}Fe_{0.80}^{\bullet}\right)_A\left[Li_{0.25}''Zn_{0.30}'Fe_{1.45}^{\times}\right]_B\left(O_4^{\times}\right)_O}_{\text{lithium}-\text{zinc ferrite}}$$

for x=1.00:

$$\left(Zn_{0.09}^{2+}Fe_{0.91}^{3+}\right)_A\left[Zn_{0.91}^{2+}Fe_{1.09}^{3+}\right]_B\left(O_4^{2-}\right)_O + \underbrace{V_A''[V_2''']_B\left(V_4^{\bullet\bullet}\right)_O}_{\text{spinel antistruct ure}} \rightarrow$$

$$\rightarrow \underbrace{\left(Zn_{0.09}^{\times}Fe_{0.91}^{\bullet}\right)_A\left[Zn_{0.91}'Fe_{1.09}^{\times}\right]_B\left(O_4^{\times}\right)_O}_{\text{zinc ferrire}}$$

In general, the antistructural modeling for mixed Li-Zn ferrite can be written as follows:

$$\left(Li^{+}_{0.5-0.5x-y}Zn^{2+}_{x-z}Fe^{3+}_{0.5-0.5x+y+z}\right)_A\left[Li^{+}_{y}Zn^{2+}_{z}Fe^{3+}_{2-y-z}\right]_B\left(O^{2-}_{4}\right)_O + V''_A[V'''_2]_B\left(V^{\bullet\bullet}_4\right)_O \rightarrow$$
$$\rightarrow\left(Li'_{0.5-0.5x-y}Zn^{\times}_{x-z}Fe^{\bullet}_{0.5-0.5x+y+z}\right)_A\left[Li''_{y}Zn'_{z}Fe^{\times}_{2-y-z}\right]_B\left(O^{\times}_{4}\right)_O$$

The crystalloquasichemical composition of the Li-Zn ferrites system is shown in Table 2. It can be seen that the spinel ferrites contain positively charged $Fe^{\bullet}_A$ and negatively charged Zn'_B, Li'_A and Li''_B active centers on the surface of the crystalline lattice. With an increase in Zn^{2+} content, the concentrations of active centers in tetrahedral (A) and octahedral (B) sublattices are changed (Fig. 4). From Figure 4 we can see that the concentration of negatively charged donor active centers Li'_A and Li''_B decreases with the Zn^{2+} concentration increase, while the concentration of negatively charged donor active centers Zn'_B increases with the Zn^{2+} concentration increase. The concentration of positively charged acceptor active centers $Fe^{\bullet}_A$ first decreases up to x = 0.70 but then increases. Crystalquasichemical formulas give us clear information about active centers: Zn^{2+}_A and Fe^{3+}_B are not active centers in any chemical reactions because they have an effective zero charge, while Li^{+}_A, Fe^{3+}_A, Li^{+}_B, and Zn^{2+}_B will be an active center in the catalysis, adsorption or other processes in a gaseous or liquid environment.

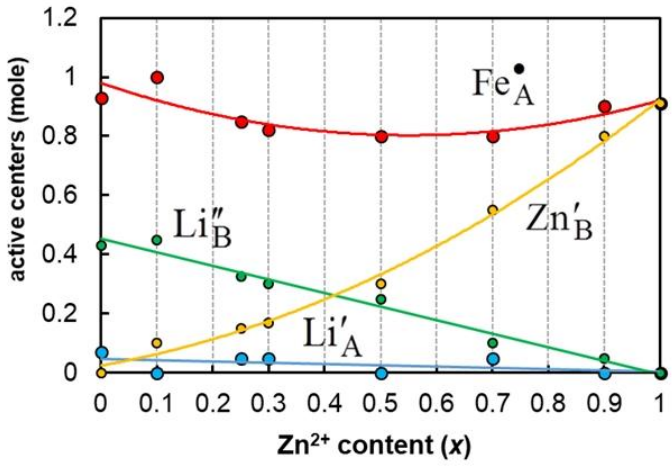

Figure 4. The concentration of active centers in tetrahedral (A) and octahedral (B) sites as a function of Zn^{2+}content (x).

Table 2. Donor and acceptor active centers on the surface of the studied Li-Zn ferrites with Zn content (x).

x (Zn^{2+})	Chemical formula	Crystalquasichemical composition
0.00	$Li_{0,5}Fe_{2,5}O_4$	$\left(Li'_{0.07}Fe^{\bullet}_{0.93}\right)_A\left[Li''_{0.43}Fe^{\times}_{1.57}\right]_B\left(O^{\times}_4\right)_O$
0.10	$Li_{0,45}Zn_{0,1}Fe_{2,45}O_4$	$\left(Fe^{\bullet}_{1.00}\right)_A\left[Li''_{0.45}Zn'_{0.10}Fe^{\times}_{1.45}\right]_B\left(O^{\times}_4\right)_O$
0.25	$Li_{0,375}Zn_{0,25}Fe_{2,375}O_4$	$\left(Li'_{0.05}Zn^{\times}_{0.10}Fe^{\bullet}_{0.85}\right)_A\left[Li''_{0.325}Zn'_{0.15}Fe^{\times}_{1.525}\right]_B\left(O^{\times}_4\right)_O$
0.30	$Li_{0,35}Zn_{0,30}Fe_{2,35}O_4$	$\left(Li'_{0.05}Zn^{\times}_{0.13}Fe^{\bullet}_{0.82}\right)_A\left[Li''_{0.30}Zn'_{0.17}Fe^{\times}_{1.53}\right]_B\left(O^{\times}_4\right)_O$
0.50	$Li_{0,25}Zn_{0,5}Fe_{2,25}O_4$	$\left(Zn^{\times}_{0.20}Fe^{\bullet}_{0.80}\right)_A\left[Li''_{0.25}Zn'_{0.30}Fe^{\times}_{1.45}\right]_B\left(O^{\times}_4\right)_O$
0.70	$Li_{0,15}Zn_{0,7}Fe_{2,15}O_4$	$\left(Li'_{0.05}Zn^{\times}_{0.15}Fe^{\bullet}_{0.80}\right)_A\left[Li''_{0.10}Zn'_{0.55}Fe^{\times}_{1.35}\right]_B\left(O^{\times}_4\right)_O$
0.90	$Li_{0,05}Zn_{0,9}Fe_{2,05}O_4$	$\left(Zn^{\times}_{0.10}Fe^{\bullet}_{0.90}\right)_A\left[Li''_{0.05}Zn'_{0.80}Fe^{\times}_{1.15}\right]_B\left(O^{\times}_4\right)_O$
1.0	$ZnFe_2O_4$	$\left(Zn^{\times}_{0.09}Fe^{\bullet}_{0.91}\right)_A\left[Zn'_{0.91}Fe^{\times}_{1.09}\right]_B\left(O^{\times}_4\right)_O$

3.3 SEM analysis

Fig. 5 depicts the representative SEM micrographs (left panel, inset: SEM images with low magnification), and particle size distribution (right panel) for the studied samples with Zn-content x = 0.0, 0.25, 0.7. SEM images illustrate that non-homogeneous particle size dispersal is also seen in SEM images, as was also seen in [63], and particle

agglomeration is ascribable to the magnetic nature of the samples. Dissimilarity in sample microstructure specifies the presence of different metal ions: Li, Zn, and Fe plays a crucial role in on microstructure of the prepared spinel ferrite samples. Particle size distribution shows notable dependence on Zn-content and mean particle size ranges between 120 to 212 nm. The observed Zn-content-dependent broadening of distribution width, ranging between 25–241 nm is observed. It is an essential indicator and provides the basis to assess the particle homogeneity, and lower distribution width corresponds to less scattered particle size, and volume.

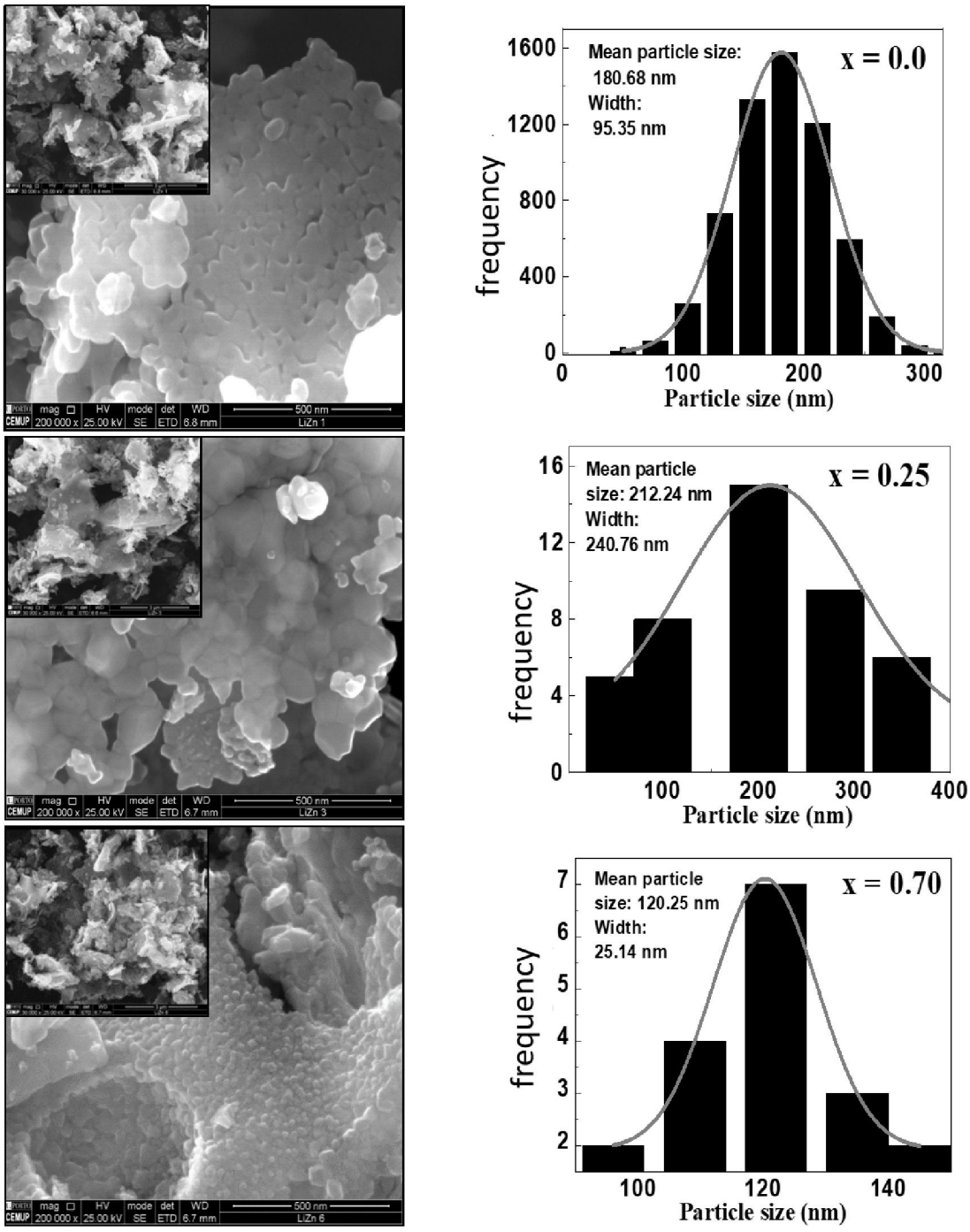

Figure 5. SEM images of the studied Li-Zn ferrites with Zn content (x): x = 0.0, 0.25, 0.70, and particle size distribution obtained from SEM images. Insets: low magnification SEM images.

3.4 Magnetic properties

Fig. 6 shows the hysteresis loops of studied samples showing Zn-content dependent variation of saturation magnetization ($M_{s(exp.)}$), while inset gives the variation of experimental saturation magnetization $M_{s(exp.)}$ at 300 K, theoretical $M_{s(t)}$ at 0 K of the studied samples. Fig. 6(inset) depicts the variation of $M_{s(exp.)}$ and $M_{s(th.)}$ with Zn-content, and the dissimilar trend shows that magnetism in the studied samples is governed by Yafet-Kittel (Y−K) three-sub-lattice model [8, 37], shown by non-zero canting angle (α_{Y-K}), range between 7.02 – 39.21 degree. It is of value to note that, saturation magnetization gets modified but it also gets affected by the presence of the anti-ferromagnetic Fe_2O_3 phase. samples with x = 0.9; 1.0, as seen in Fig. 6.

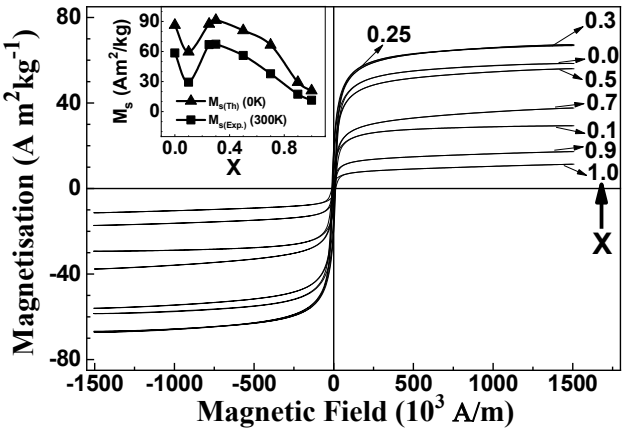

Figure 6. Hysteresis loops of studied samples. Inset: Variation of experimental saturation magnetization $M_{s(exp.)}$ at 300 K (or just M_s), theoretical $M_{s(t)}$ at 0 K of the studied samples with Zn-content (x).

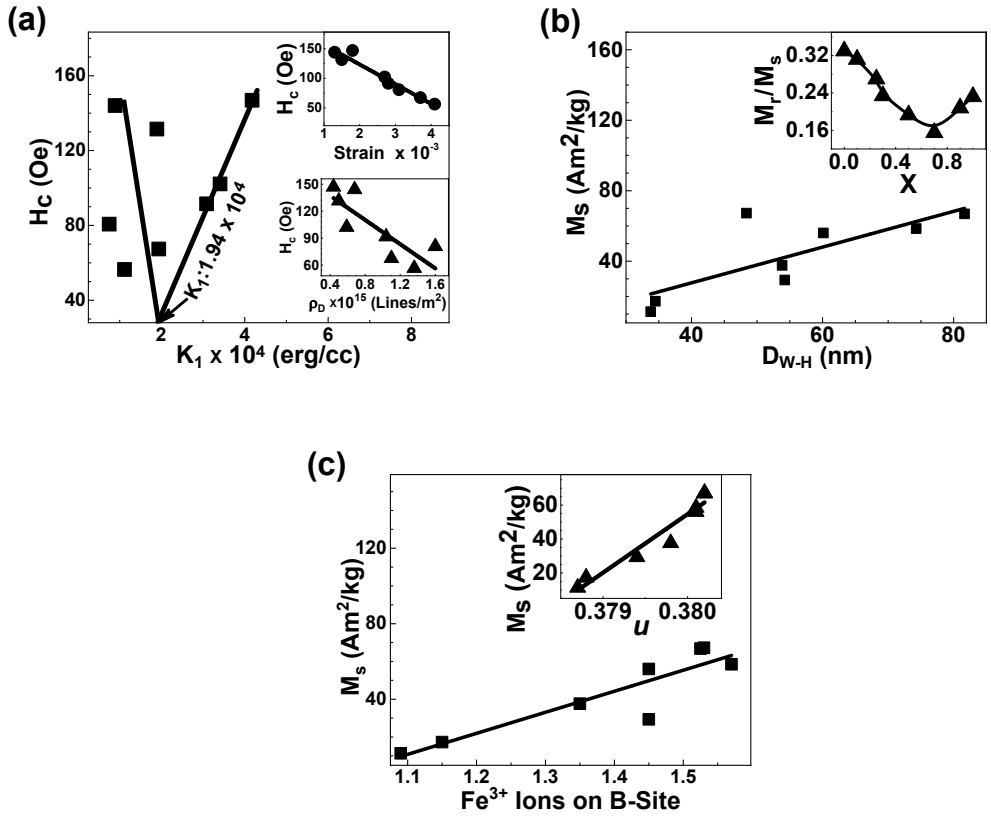

Figure 7. (**a**) Variation of H_c with K_1 (Upper inset: variation of H_c with strain; Lower inset: variation of H_c with ρ_D), (**b**) Variation of M_s with $D_{W\text{-}H}$ (Inset: Variation of M_r/M_s with Zn-content), (**c**) Variation of M_s with Fe^{3+} ions on B-site (Inset: Variation of M_s with *u*).

Fig. 7 a depicts the dependence of H_c with K_1. A perusal of Fig. 7a shows two-slope behavior between H_c and K_1. It should be noted that with the variation of Zn- between 0.0 to 1.0, K_1 decreases linearly from 4.18×10^4 to 0.75×10^4 ergs/cc. Two-slope behavior is understood as follows: i) Initial decrease of H_c with K_1 is ascribable to increase in Zn-content, ii) Subsequent increase of H_c is ascribable to decrease of $D_{W\text{-}H}$ with Zn-content (see Fig. 2a), and domination of surface effects (see Fig. 2c, where with increasing Zn-content specific surface area increases), iii) observed cross-over of the slope corresponds to Zn-content = 0.5, where there is highest occupation of Zn-content (0.20) on A-site (see Table 1), leading to sharp increase of K_1. The upper inset shows that

with increasing strain, H_c decreases, described by the experimental relation: $H_c = 189.76 - 33.21$ [Strain], ascribable to Zn-migration on A-site, with concurrent reduction of K_1. The lower inset of Fig. 7a depicts a linear decrease of H_c with dislocation density, which is described by the following experimental relation: $H_c = 164.23 - 67.47$ [ρ_D]. The decrease of H_c is understood by the fact that, as with decreasing $D_{W\text{-}H}$, there is an increase of ρ_D.

Fig. 7b shows a linear increase of M_s with $D_{W\text{-}H}$, described by the experimental relation: $M_s = 1.015$ [$D_{W\text{-}H}$] -12.872, is ascribable to spin disorder or spin canting effects, as was also observed in [64-65], evident by the observed as non-zero canting angle ($\alpha_{Y\text{-}K}$), range between 7.02 – 39.21 degree. Fig. 7b(inset) shows the Zn-content dependence of M_r/M_s, which varies between 0.155 – 0.330, ascribable to stronger interactions among multi-domain grains, and surface spin canting [66].

Fig.7 c shows linear increase presents a linear variation of saturation magnetization at 300 K 'M_s' with Fe^{3+} ions on the B site described by the experimental equation: $M_s - 111.408$ [Fe^{3+} ions on B-site] −111.747, clearly demonstrates the role of cationic distribution in shaping magnetic properties, seem to be explained by Neel two sub-lattice model [56]. According to Néel's model, the cationic magnetic moments on A and B sites are allied anti-parallel to each other forming a collinear structure with certain resultant magnetization $M = M_B - M_A$, where M_A and M_B are, respectively, the magnetic moment of A and B sites. Nevertheless, it should be noted that a non-zero canting angle ($\alpha_{Y\text{-}K}$), ranging between 7.02 – 39.21 degrees, reveals the presence of surface spin canting, thus the magnetism of the studied samples is better explained by Yafet-Kittel (Y−K) three sub-lattice model [8, 37]. Fig. 7c(inset) shows a linear increase of M_s with Oxygen parameter u, described by the fitting equation: $M_{s(exp.)} = 34512.846$[u] −13060.192, is ascribable to increased disorder in the studied specimens as was also reported in [5, 56].

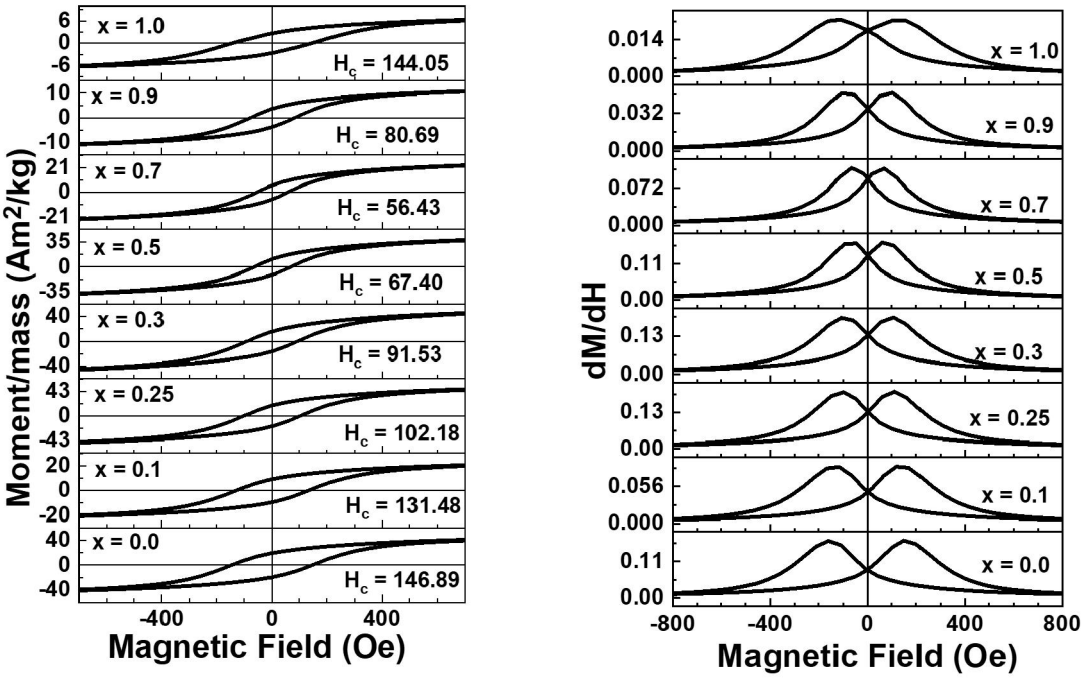

Figure 8. Hysteresis loops (left panel), and corresponding first derivative of magnetization 'dM/dH' (right panel).

Table 3. H_c, FWHM of 1st derivative peak, switching field distribution (SFD), and a peak height of 1st derivative.

x	H_c (Oe)	FWHM or ΔH of 1st derivative peak (Oe)	SFD ($\Delta H / H_C$)	Peak Height of 1st derivative
0.0	146.89	756.42	5.15	0.10
0.1	131.48	707.92	5.38	0.05
0.25	102.18	619.71	6.06	0.13
0.3	91.53	610.59	6.67	0.13
0.5	67.40	504.06	7.48	0.12
0.7	56.43	464.05	8.22	0.08
0.9	80.69	523.59	6.49	0.03
1.0	144.05	683.93	4.75	0.01

Fig. 8 depicts hysteresis loops (left panel), and the corresponding first derivative dM/dH (right panel). Perusal of Fig. 8 shows that dM/dH shows double peak behavior, and describes the competition between exchange coupling, strong dipolar interaction [67-

68]. Table 3 gives the Zn-content dependence of full width at half maxima (FWHM) of 1st derivative peak, switching field distribution (SFD), and peak height of 1st derivative. Broader peaks (see Table 3) range between 467.05 Oe to 765.42 Oe stipulating nanocrystalline samples containing dislocations and defects in the crystal [6]. Peak broadness is also linked with the stability of the material: the broader the peak of the first derivative, the more stable the structure of the nanoparticle [69]. A perusal of Table 3 shows that the peak height varies between 0.01 – 0.13. Modification of dM/dH peak height indicates that the studied samples have a good magnetic state of crystalline cubic spinel structure [70]. Switching field distribution 'SFD' is an essential magnetic parameter, and it measures the energy barrier distribution in a nanoparticle system and is accompanied by a distribution of particle coercivity [69-71]. Systems with small SFD and high H_c are appropriate for high-density recording [72], and the smaller the distribution of the switching field, is better suited for magnetic recording. For the studied samples the SFD range is between 4.75 and 8.22. Thus, among the studied samples (e.g., Zn-content = 1.0) with, the lowest SFD (4.75) and high Hc (144.05) show the prospective application in magnetic recording, whereas sample (Zn-content = 0.7) with the lowest H_c (56.43 Oe), highest SFD (8.22), would be of use for targeted drug delivery applications [73]. It is of value to note that, the switching field distribution 'SFD' values have a strong connection with the particle size distribution since particles with different shapes, and sizes would tend to reverse at different magnetic field strengths. Consequently, in the studied samples, the observed variation of SFD values is ascribable to the variation of the particle size distribution [69], and thus particle size distribution obtained from SEM data, is meaningful for enhanced understanding of the magnetic behavior of the studied samples, where the particle size distribution is different (see Fig. 5), and the mean particle size range between 120 nm to 212 nm.

4. Conclusions

To summarize, single-phase nanocrystalline Li-Zn ferrite samples were synthesized by sol-gel auto-combustion technique. XRD confirms the formation of single-phase nanocrystalline samples with crystalline sizes of 34 – 82 nm. Changes in a_{exp}, ρ_{xrd} with Zn content are ascribed to the difference in ionic radii and density of Li^{+} ions and Zn^{2+} ions. The dependence D *vs.* H_c reveals the single domain structure of the studied ferrite. Observed values of M_s and H_c signify the soft character of studied samples. SEM images reveal the presence of non-uniform particle distribution. An antistructural model featuring the surface of Li-Zn ferrites was proposed, which can be applied for the explanation and prediction of chemical, adsorption, catalytic, and other properties of spinel ferrites. It was shown that the nature of surface active centers depends on the kind and placement of cations in the spinel structure. Spinel ferrite contains positively charged ($Fe_A^{\bullet}$) and negatively charged (Zn_B', Li_A' and Li_B'') active centers on the surface of the crystalline lattice. With an increase in Zn content, the concentration of active centers in tetrahedral (A) and octahedral (B) sublattices is changed. Fraction of Li_B'' and $Fe_A^{\bullet}$ decreases, while the concentration of Zn_B' increases with Zn content, ascribed to migration of Li^{+} and Zn^{2+} cations among A and B-sites. Zn content-dependent M_s and $M_{s(t)}$ verify the role of cationic distribution in describing magnetic properties.

Acknowledgments:

This work is supported by Seed money grant: No. Dev/Seedmoney2.0/2020-21/649, 20 Jan. 2022 of Devi Ahilya University, Indore (India). The authors thank Dr. M. Gupta, UGC-DAE CSR, Indore for the XRD data. SNK acknowledges gratefully for an invited professor stay (Nov. 2016), ENS Paris-Saclay, Cachan, France.

Authors' contributions: SNK has conceptualized the work, synthesized the ferrite samples and has participated in XRD (*With RV, CP, SSM*), SEM (*with JP*), and VSM measurements (*with FM*). SNK (with RV, CP and SSM) analyzed the XRD data. SNK and FM analyzed VSM data. JP and SNK analyzed SEM data. TT and SNK contributed to the preparation and proofreading of the manuscript. TT described the antistructural modelling. All the authors have read and approved the final version of the manuscript.

References:

[1] T. Tatarchuk, et al. *Nanophysics, Nanomaterials, Interface Studies, and Applications. NANO 2016. Springer Proceedings in Physics* **195**, 305 (2017). doi:10.1007/978-3-319-56422-7_22

[2] P. Tiwari, *et al. Mol. Cryst. Liq. Cryst.* 699, (2020).doi:10.1080/15421406.2020.1732537

[3] S. Panchal, *et al., AIP Advances* 6, 055930 (2016). Doi:10.1063/1.4944517

[4] D. S. Mathew, *et al., Chem. Eng. J.* 129, 51 (2007). doi:10.1016/j.cej.2006.11.001

[5] C. Parmar, *et al. ECS J. Solid State Sci. Technol.* **11,** 053015 (2022). doi:10.1149/2162-8777/ac6f1b

[6] T. Dippong, *et al. Nanomaterials* **10**,580 (2020). doi:10.3390/nano10030580

[7] P. Tiwari, et al. Nanophotonics, Nanooptics, Nanobiotechnology, and Their Applications, Springer Proceedings in Physics 222, 439 (2019). doi:10.1007/978-3-030-17755-3_29

[8] S. N. Kane, *et al. Mater. Today Proc.* **32**, 358 (2020). doi:10.1016/j.matpr.2020.02.036

[9] P. Tiwari, *et al., Hyperfine Interactions* **242**, 51 (2021). doi: 10.1007/s10751-021-01781-z

[10] P. Tiwari, *et al. AIP Conf. Proc.***2142**, 150018 (2019). doi:https://doi.org/10.1063/1.5122567

[11] X. Cao, *et al. J. Magn. Mag. Mater*. **321** (18), 2896 (2009). doi:10.1016/j.jmmm.2009.04.049

[12] K. Chae, *et al. J. Magn. Mag. Mater.* **324** (18), 2701 (2012). doi:10.1016/j.jmmm.2012.03.024

[13] S. Balamurugan, *et al. J. Mater. Sci: Mater. Electron.* 28, 18610 (2017). doi:10.1007/s10854-017-7810-9

[14] Y. Zheng, *et al., Compos. Part A: Appl. Sci. Manufactur.* **95**, 237 (2017). doi:10.1016/j.compositesa.2017.01.015

[15] X. Cai, *et al., J. Alloys. Compd.* **657**, 608 (2016). doi:10.1016/j.jallcom.2015.10.153

[16] I. Soibam, *et al., Phys. B: Cond. Matter.* **405** (9), (2010). 2181. doi:10.1016/j.physb.2010.01.131

[17]. L. R. Gonsalves, *et al. J. Mater. Sci: Mater. Electron.* **33**, 20144 (2022). doi: 10.1007/s10854-022-08833-2

[18] S. Misra, *Mater. Res. Bull.* **91**, 203 (2017). doi:10.1016/j.materresbull.2017.03.039

[19] P. Thakur *et al., J. Magn. Mag. Mater.* **432**, 208 (2017). doi:10.1016/j.jmmm.2017.01.081
[20] M.K. Abbas *et al.*, *Ceram Int* **43** (7) 5524 (2017). doi:10.1016/j.ceramint.2017.01.075
[21] H. Kumar, *et al., Superlattices Microstruct.* **109,** 296 (2017). doi:10.1016/j.spmi.2017.05.001
[22] M. Junaid, *et al., J. Magn. Mag. Mater.* **419,** 338 (2016). doi:10.1016/j.jmmm.2016.06.043
[23] H.M.T. Farid, *et al. Ceram. Int.* **43** (9), 7253 (2017). doi:10.1016/j.ceramint.2017.03.016
[24] Y. Liu, *et al., J. Magn. Mag. Mater.*, 349, 57 (2014). doi:10.1016/j.jmmm.2013.08.054
[25] Y. Wang, *et al. J. Magn. Magn. Mat.* **398,** 90 (2016). doi:10.1016/j.jmmm.2015.09.044
[26] M. AsifIqbal, *et al. J. Alloys. Compd.* **692**, 322 (2017). doi:10.1016/j.jallcom.2016.09.049
[27] A. Manzoor, *et al. J. Alloys. Compd.* **710**, 547 (2017). doi:10.1016/j.jallcom.2017.03.154
[28] Z. Gilani, *et al. Physica E Low Dimens. Syst. Nanostruct.* **73,** 169 (2015). doi:10.1016/j.physe.2015.06.001
[29] E. Ateia, *et al.* Appl. Phys. A. **123**, 312 (2017). doi:10.1007/s00339-017-0948-8
[30] X. Jiang, *et al., J. Magn. Mag. Mater.* **321** (2), 52 (2009). doi:10.1016/j.jmmm.2008.07.044
[31] M. Ahmed, *et al., Phys.B: Cond. Matter.* **530**, 195 (2018). doi:10.1016/j.physb.2017.10.125.
[32] H. Ghayour, *et al., J. Phys. Chem. Solids* **111,** 464 (2017). doi:10.1016/j.jpcs.2017.08.018
[33] G. Datt, *et al.*, J. Appl. Phys., **122**, 034102 (2017). doi:10.1063/1.4990275
[34] T. Tatarchuk, *et al., J. Alloys. Compd.* **731**, 1256 (2018). doi:10.1016/j.jallcom.2017.10.103
[35] S. Gawas, et al., *Mater. Chem. Front.* (2018). doi:10.1039/C7QM00437K
[36] K. Babu, *et al., J. Magn. Mag. Mater.* **434**, 118 (2017). doi:10.1016/j.jmmm.2017.03.044
[37] P. Reddy, *et al., Phys. B. Cond. Matter.* **405**, 1852 (2010). doi:10.1016/j.physb.2010.01.062
[38] S. Sutradhar, *et al., J. Magn. Mag. Mater.* **324** (7), 1317 (2012). doi:10.1016/j.jmmm.2011.11.019
[39] I. Szczygieł, *et al., J. Alloys Compd.* **604**, 1 (2014). doi:10.1016/j.jallcom.2014.03.109.
[40] A. Hernández-Hernández, *et al., Mater. Chem. Phys.* **205**, 113 (2018). doi:10.1016/j.matchemphys.2017.11.009
[41] K. Kombaiah, *et al., Mater. Chem. Phys.* **204**, 410 (2018). doi:10.1016/j.matchemphys.2017.10.077
[42] M. Junaid, *et al., Ceram. Int.,* **48** (15), 21610 (2022). doi:10.1016/j.ceramint.2022.04.134.
[43] K. Batoo, *et al., Nanoscale Res. Lett.,* **7**, 112 (2012). doi:10.1186/1556-276X-7-112
[44] G. Aravind, *et al., J. Nanostruct. Chem.* **5**, 77 (2015). doi:10.1007/s40097-014-0138-6

[45] C. Sun, *et al., Phys. B. Cond. Matter.* **391** (2), 335 (2007). doi:10.1016/j.physb.2006.10.016

[46] N. Borhan, *et al., J. Supercond. Nov. Magn.* **27**, 1483 (2014). doi:10.1007/s10948-013-2450-7

[47] I. Soibam, *et al., J. Alloys. Compd.* **475** (1–2), 328 (2009). doi:10.1016/j.jallcom.2008.07.011

[48] M. Ruiz, *et al., Phys. B. Cond. Matter.* **407** (16), 3274 (2012). doi:10.1016/j.physb.2011.12.085

[49] S. Mazen, *et al., Powd. Tech.* **317**, 339 (2017). doi:10.1016/j.powtec.2017.05.011

[50] X. Sun, *et al., Ferroelectrics* **489** (1), 19 (2015). doi:10.1080/00150193.2015.1070652

[51] E. F. Bertaut, Comptes Rendus Hebdomadaires des Seances de I'Academie des Sciences **230**, 213 (1950).

[52] A. R. Tanna, *et al.,* World Academy of Science, Engineering and Technology, Int. J. of Physical and Mathematical Sciences **7** (3), 334 (2013). Doi: 10.5281/zenodo.1333917

[53] S. N. Kane, *et al., Hyperfine Interactions* **244**,3 (2023). doi: 10.1007/s10751-022-01814-1

[54] C.A. Schneider, *et al., Nat. Methods* **9,** 671 (2012). doi:10.1038/nmeth.2089

[55] S. Mallesh, *et al., AIP Adv.* 7, 056103 (2017). doi: /10.1063/1.4975355

[56] S. N. Kane, *et al., Interactions* **245**, 36 (2024). doi: 10.1007/s10751-024-01881-6

[57] B. Antic, *et al., J. Phys. B: Cond. Matter* **25**, 086001(2013). doi:10.1088/0953-8984/25/8/086001

[58] D. Vollath, Nanoparticles – Nanocomposites –Nanomaterials An Introduction for Beginners, p. 30. Wiley-VCH Verlag, Weinheim (2013)

[59] J. Smit, H.P.J Wijn, Ferrites, pp. 136–149. Philips Technical Library, Eindhoven p (1959)

[60] T. Tatarchuk, *et al., J. Alloys. Compd.* **694**, 777 (2017). doi:10.1016/j.jallcom.2016.10.067

[61] R. Kumar, *et al., J. Solid. State. Electrochem.* (2018). doi:10.1007/s10008-017-3865-z

[62] K. Sickafus, *et al.,* J. Am. Ceram. Soc. **82**, 3279 (1999). doi:10.1111/j.1151-2916.1999.tb02241.x

[63] S. N. Dolia *et al., Radiat. Eff. Defects Solids.* **166** (8–9), 558 (2011). doi: 10.1080/10420150.2011.553232

[64] R. S. Yadav *et al., Adv. Nat. Sci: Nanosci. Nanotechnol.* **8**, 045002 (2017). doi: 10.1088/2043-6254/aa853a

[65] M. Chithra *et al., J Mater Sci: Mater. Electron***. 34**, 806 (2023). doi:10.1007/s10854-023-10241-z

[66] G. Muscas *et al., Nanoscale* 7 13576 (2015). doi:10.1039/c5nr02723c

[67] A. G. Kolhatkar *et al., Int. J. Mol. Sci.* 14 (8), 15977 (2013). doi: 10.3390/ijms140815977

[68] E. E. Ateia *et al., J. Mater. Sci: Mater. Electron.* 33 (11), 8958 (2022). doi: 10.1007/s10854-021-07008-9

[69] S. Kumar *et al., Mater. Sci. Eng. B.* **272**, 115362 (2021). Doi: 10.1016/j.mseb.2021.115362

[70] I. P. Muthuselvam *et al., J. Magn. Magn. Mater.* **322** (7), 767 (2010). doi:10.1016/j.jmmm.2009.10.057

[71] D. Jiles, Introduction to Magnetism and Magnetic Materials (Chapman and Hall, New York, 1991). DOI 10.1007/978-1-4615-3868-4

[72] J. C. Lodder, Handbook of Magnetic Materials, **11**, 291 (1998). Doi:10.1016/S1567-2719(98)11006-5

[73] S. Kumar *et al., J. Inorg. Organomet. Polym.* **31** (2), 528 (2021). doi: 10.1007/s10904-020-01764-7